AJNR

Blood flow dynamics in the vertebrobasilar system: correlation of a transparent elastic model and MR angiography.

B W Chong, C W Kerber, R B Buxton, L R Frank and J R Hesselink

AJNR Am J Neuroradiol 1994, 15 (4) 733-745
http://www.ajnr.org/content/15/4/733

Blood Flow Dynamics in the Vertebrobasilar System: Correlation of a Transparent Elastic Model and MR Angiography

Brian W. Chong, Charles W. Kerber, Richard B. Buxton, Lawrence R. Frank, and John R. Hesselink

PURPOSE: To describe the flow patterns in a model of the vertebrobasilar artery and use these observations to explain the appearance of the flow on the MR images. **METHODS:** We created an anatomically precise, transparent elastic model of the human vertebrobasilar artery containing a basilar tip aneurysm and perfused the model with non-Newtonian fluid which has similar rheologic properties to blood. Flow patterns in the vessels were directly observed. MR angiogram images were obtained with commercially available two-dimensional time-of-flight, three-dimensional time-of-flight, and 3-D phase-contrast MR angiographic pulse sequences, and they were correlated with the directly seen flow patterns. Quantitative flow velocity measurements were performed with 2-D cine phase-contrast MR angiography and correlated with the flow measured with an electromagnetic flow meter. **RESULTS:** Visualization studies showed the dye stream patterns in the vertebrobasilar arteries to be extremely complex and variable. During the MR experiments we found that often the same segment of a vessel could appear very different depending on the pulse sequence. In some instances, the model experiments helped to explain the MR appearance of the vessels. Flow profiles measured with 2-D cine phase contrast were found to be consistent with those measured directly with an electromagnetic flow meter. **CONCLUSION:** Clear elastic models can be used to duplicate the flow in human cranial vessels and thus provide a unique means to observe these flow patterns directly. The flow patterns helped to explain the variation in appearance of the vessels and the artifacts with different MR angiography pulse sequences. The artifacts depend on both the geometry of the vessel and the flow pattern within it. Two-dimensional cine phase-contrast MR provides temporal flow field information that is directly related to physiological information about flow volumes and velocity patterns.

Index terms: Arteries, basilar; Arteries, flow dynamics; Arteries, magnetic resonance angiography (MRA); Arteries, vertebral; Magnetic resonance, flow studies; Models, anatomic

AJNR Am J Neuroradiol 15:733–745, Apr 1994

It is difficult to study blood flow to the human brain in a safe, accurate, and noninvasive manner for a number of reasons. In vivo manipulation of flow is not well tolerated by the organism. Existing models do not accurately duplicate the anatomy and physiology of in vivo conditions (1–6). Noninvasive techniques such as Doppler ultrasound are limited when assessing the carotid and vertebral systems because these vessels lie in bone for much of their course and change direction frequently. Magnetic resonance (MR) angiography (MRA) has been used to depict the vascular anatomy and to quantitate flow with some promise (7–18). When flow is complex, as in the vessels of the human brain, there are limitations inherent to the MR acquisition and reconstruction method which result in inaccurate depiction of flow. Each of the many pulse sequences has its own set of artifacts that depend on both the geometry of the vessel and the flow pattern within it. We must understand the flow physiology of the cranial vessels to understand the origin of the artifacts and the limitations of MRA.

Our objective was to describe the flow patterns in the vertebrobasilar artery model and use these observations to explain the appearance of the

Received March 24, 1993; accepted pending revision June 14; revision received July 7.

This work was supported by an ASNR-Berlex research grant.

From the Department of Radiology, University of California San Diego Medical Center.

Address reprint requests to Brian W. Chong, MD, Department of Radiology, University of California-Davis School of Medicine, Ticon II Building, 2516 Stockton Blvd, Scaramento, CA 95817.

AJNR 15:733–745, Apr 1994 0195-6108/94/1504-0733

flow on the MR images. We observed the paths of dye streams in the flowing fluid and correlated these observations with the appearance of the vessels on commercially available flow-sensitive MR pulse sequences.

Materials and Methods

This study required: 1) the creation of anatomically precise, transparent viscoelastic models; 2) the perfusion of those models with a non-Newtonian fluid having the same rheologic properties as human blood; 3) the perfusion of the system with a physiologic flow profile, at physiologic Reynolds numbers; 4) the direct observation and analysis of the various dye streams in the models; and 5) the study of these same models in the MR scanner, correlating the findings and especially the artifacts with the directly seen flow patterns.

Preparation of the Model

Fresh adult human cadavers were obtained, the brachiocephalic vessels were exposed, and the arteries to the head and neck were infused with Batson corrosion compound. After the compound cured, the head was removed and dissolved in concentrated alkali. The arterial lumen castings that remained were then encased in a molding material, and the mold was opened after it had cured. Wax was then injected into the mold cavity and removed. That wax, which then reproduced the original arterial lumen, was next dipped in a clear silicone. Finally, the wax was removed. The change in dimension from the original casting was approximately 0.1%. Details of the preparation have been reported elsewhere (19).

Experimental Flow System

The model was then placed in a circuit of flowing fluid. The model flow studies and the MR studies were performed at separate times but using the same apparatus. The tubes were long enough that the pump could be placed outside the MR scan room. All tubing lengths and diameters were kept constant throughout all of the observations. Two straight, rigid wall polycarbonate tubings, 30 vessel diameters in length, connected the model into the circuit. An electromagnetic flow meter (model FM 501, Carolina Medical Electronics, King, NC) was placed 20 cm proximal to the straight tube. The flow meter was calibrated by collecting samples of the fluid that passed through the system in a known period of time. Immediately proximal to the flow meter, we placed a T junction leading to a latex expansion chamber. We varied the length of the latex expansion chamber while observing the flow meter to create a flow wave similar to that in the cranial circulation (Fig 1). Fluid flow was provided by a Harvard pump (model 1421, Harvard Apparatus, South Natwick, Mass). The circulating fluid was a solution of sodium chloride and xanthan gum. This fluid matches the rheologic properties of human blood (4).

Flow Visualization Studies

Primary observations were made at physiologic flows of approximately 240 mL/sec, which gave a Reynolds number of 200. We placed 30-gauge needles into various points in the flow and injected two different colored isobaric dyes into the flowing fluid. We recorded the results on super VHS television and also on 35-mm film. The experimental system is shown in Figure 2.

MR

MR was performed on a 1.5-T scanner (General Electric, Milwaukee, Wis) using a quadrature head coil. We placed the model into the magnet embedded in a horizontal open-

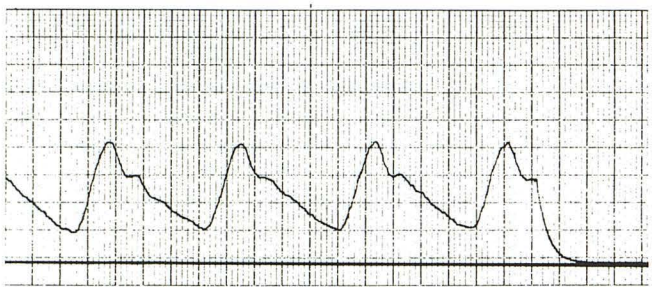

Fig. 1. Flow (not velocity) profile recorded in the system just before the straight tubing. Note that end diastolic flow is about 30% of peak systolic flow. The rate is 60 per minute.

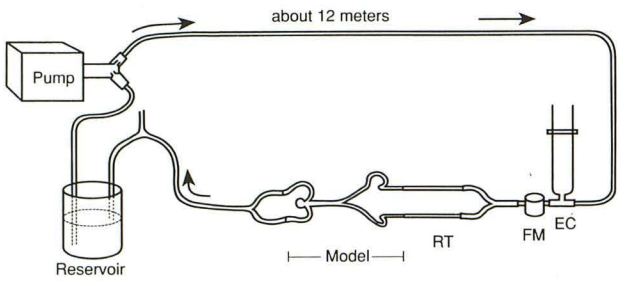

Fig. 2. The essential parts of the circulating system. The pump provides pulsatile flow into the tubing. The tubing is long enough that the pump can be placed outside the MR scanner room. A T junction leads to a latex expansion chamber (*EC*). The chamber stores energy, modifying the pump's pulse wave to that seen in human cranial arteries. An electromagnetic flow meter (*FM*) measures global flow and also gives an instantaneous flow profile. Next, rigid straight polycarbonate tubes (*RT*) eliminate upstream flow disturbances induced by the curved tubings, couplings, and measuring devices, and present the model with a clean velocity pattern. The model is placed into the system and back-lighted for the visual recording devices. Thirty-gauge needles are placed through the silicone vessel to deliver isobaric dye streams. Tubing carries the fluid from the model to a Y junction. The open upper limb of the Y junction prevents siphoning effects; the height of the Y determines the pressure in the system.

TABLE 1: MRA parameters

Parameter	2-D Time-of-Flight	3-D Time-of-Flight	3-D Phase Contrast	2-D Cine Phase Contrast
Repetition time (msec)	45	33	24	33
Echo time (msec)	8.7 fr	5.9 fr	7.6 fr	9.3
Excitations	1	1	1	1
Flip angle	60°	20°	20°	20°
Field of view (cm)	12	12	12	12
Matrix	256 × 256	256 × 256	256 × 192	256 × 256
Section Thickness (mm)	1.5	1.0	1.0	3.0
V_{enc} (cm/sec)			100	80–150
Number of sections	64	60	60	1
Comments	First-order flow compensation	First-order flow compensation	Velocity sensitive in all directions	Velocity sensitive in superior and inferior directions

Note: fr indicates fractional echo; V_{enc}, maximum encoded velocity that will not be aliased.

topped cylinder filled with clear ultrasound gel. The tubing ran through a shielded wall. The pump was placed on the far side of the wall. The fluid contained 0.5 mM nickel chloride producing a T1 of about 2.2 seconds and a T2 of about 0.37 seconds, estimated from the spin-echo images of a sample of fluid.

The model was then examined using commercially available MRA pulse sequences which included: 1) two-dimensional time-of-flight; 2) three-dimensional time-of-flight; 3) three-dimensional phase contrast; and 4) two-dimensional cine phase contrast. Angiographic reconstructions were produced from the axial MRA images using a maximal intensity projection (20). For the time-of-flight data sets, the acquired axial images were processed directly with the maximal intensity projection algorithm. In 3-D phase contrast imaging several data sets are acquired simultaneously with different velocity sensitivity along three spatial axes. Velocity sensitivity is produced by applying bipolar field gradients along a particular axis so that the phase of the signal is proportional to the velocity. For velocity sensitivity along only one axis two image data sets are acquired in an interleaved fashion with the bipolar gradients reversed in the second sequence, so that a positive velocity produces a positive phase in the first and a negative phase in the second. In the reconstruction the two data sets are used to construct a phase-difference image in which brightness reflects velocity, which is then multiplied by the average magnitude image to produce a *weighted phase* image. In our study we chose velocity sensitivity along all three axes. The equivalent of four image acquisitions were required, and from the three phase images reflecting velocity along each axis a magnitude-weighted speed image was calculated. The maximal intensity projection algorithm is then applied to the modulus of the weighted phase image for single direction sensitivity or the magnitude-weighted speed image for velocity sensitivity in all three directions.

In addition to the MRA studies, quantitative velocity measurements were made at two sections of the model with 2-D cine phase-contrast imaging. In this technique a single section is imaged, but each phase-encoding step is repeated many times so that the data can be retrospectively sorted into 32 equal segments of the cardiac cycle based on a measured electrocardiogram recording. The result is 32 magnitude and phase images corresponding to equal segments of the cardiac cycle. The phase images are scaled so that each pixel value is the velocity at that point in the cardiac cycle. For our study an electronic switch triggered by the pump was connected to the electrocardiogram leads of the scanner to provide the reference signal. Imaging parameters are shown in Table 1. The images were then analyzed using National Institutes of Health Image software version 1.44 (National Institutes of Health, Bethesda, Md). Total volume flow (ml/min) was calculated for each time point in the pump cycle by: 1) choosing a region of interest that fully covers the vessel lumen on the images with no flow; with this model the vessel wall produces no signal, so the lumen is outlined by a dark band; and 2) summing the velocity in each pixel within the region of interest and multiplying by the area of one pixel. In principal, including pixels outside the lumen would not affect the total flow calculation because their mean velocity is zero. In practice, the finite resolution of MR images may result in a bleeding of signal into the regions outside the lumen, so this method may slightly overestimate the total flow. For this reason, care was taken to choose a region of interest that closely approximated the lumen area. For in vivo measurements the choice of a region of interest is a more important problem because the vessel wall does not provide a dark outline, and it is not possible to obtain a no-flow image.

Results

For convenience, we divided the vertebral basilar system into five segments (Fig 3). 1) The straight segment is of little interest to us rheologically, as this portion of each vertebral artery is a relatively straight tube, and we expected little artifact there. We concentrated our studies on the next four segments. 2) The cervical flexures

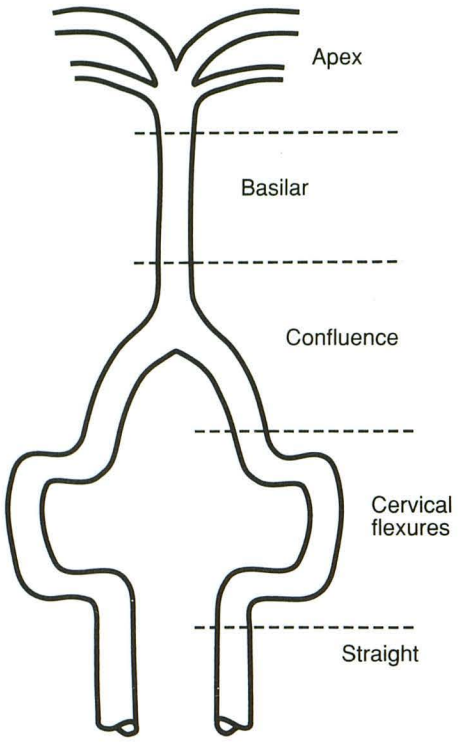

Fig. 3. Vertebrobasilar artery segments. We have arbitrarily defined the segments to aid in the description of the flow patterns. We have used terminology appropriate for rheologic description rather than the traditional anatomic description.

began where the vertebral artery left the bony canal, to pass posteriorly and laterally in the region of C-1 and C-2. Two compound curves there join one on the other. 3) The confluence is where the vessel becomes relatively straight and passes anteriorly and superiorly at about a 30° angle from the sagittal plane to the confluence of the vertebral arteries. We assumed that this segment began about 10 vessel diameters beyond the last cervical flexure and continued into the basilar artery five vessel diameters beyond the apex of the confluence. 4) The basilar segment continues cranially from the confluence until about five vessel diameters from the apex. 5) The last segment, the apex, consisted of the distal portion of the relatively straight basilar artery, the double bifurcation of the posterior cerebral arteries, the right superior cerebellar artery, and a basilar tip aneurysm. The left superior cerebellar artery was too small to be successfully constructed and therefore was not present in the model. This model did not include the posterior inferior cerebellar arteries, the anterior inferior cerebellar arteries, the posterior communicating arteries, or the small pontine perforators.

Model Flow Studies

The super VHS recordings are aesthetically pleasing and convey the flow patterns of the dye streams with greater clarity than static 35-mm photography or a narrative account could ever achieve. However, it is feasible only to describe the patterns here and display some illustrative figures.

As the dye streams entered the cervical flexures, the fluid, having mass and thus inertia, tended to continue in a straight line, crowding the dye streams toward the greater curvature, suggesting areas of relatively low flow or even reversed flow in the lesser curvatures. As dye streams converged their velocity increased. During rapid flow (systole) the dye streams struck the wall at the distal portion of the greater curvature, reflected at a sharper angle and then passed downstream to the opposite wall of the next greater curvature (see Fig 4). The point of impact on the greater curvature changed at different times in the cardiac cycle, being more distal at peak systole. The two dye streams alternated with one another in the order in which they impacted on the greater curvatures. During periods of highest flow velocity (at peak systolic flows), there were often areas of actual flow reversal within the lesser curvature. This region moved back and forth with the cardiac cycle. Internal helices almost always formed when fluid passed around any bend, as has been shown in earlier studies as well (21). The presence and character of a helix depended on how fluid entered the region from previous curves and the presence of narrowings or focal dilatations. The appearance was that of intertwining coiled springs within the vessel. Of great interest was the behavior of the springs just before systolic flow began: they seemed to compress then move forward rapidly as peak systolic flows were reached.

When the streams from each artery met at the confluence, the asymmetry of flow again caused helix formation. The dye streams from each artery then crossed to the opposite lateral wall (Fig 5). The helical flow became straight at about two to six vessel diameters downstream. Flow in the straight basilar artery was simple without significant disturbance (Fig 6).

Upon reaching the distal basilar artery and the aneurysm neck, the dye streams passed toward the right posterior aneurysm wall which was in a relatively straight line with the central dye stream. Once again the crowding of dye streams indicated

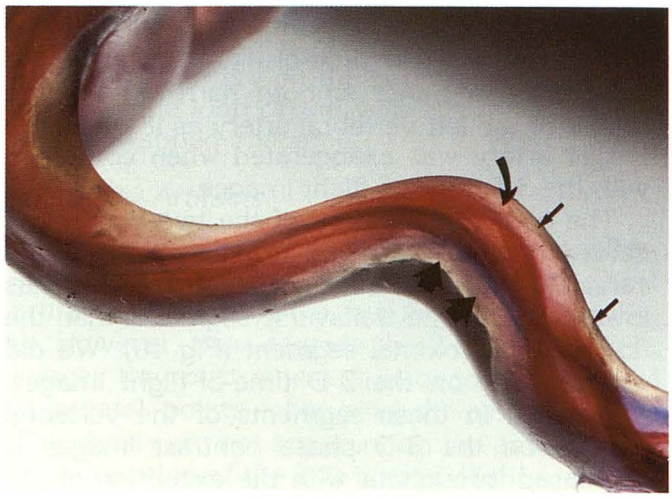

4

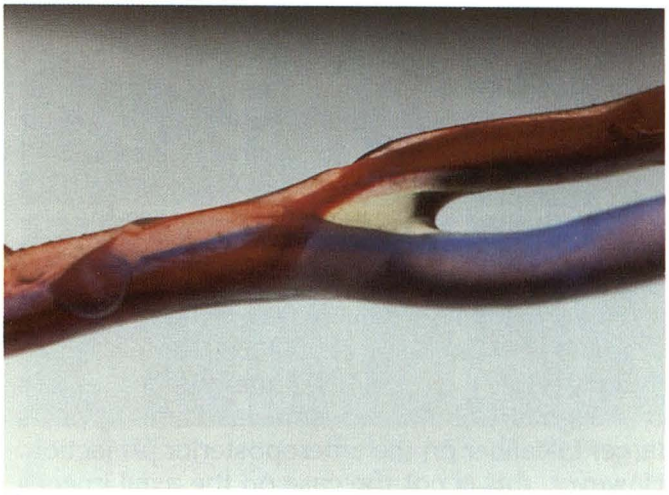

5

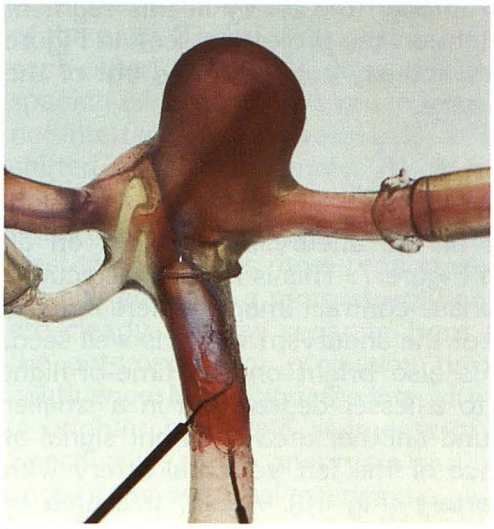

6

Fig. 4. Flow at the cervical flexures seen with isobaric dye streams. Flow consists of a series of helical swirls (*small arrows*). The dye streams strike the distal wall of the greater curvatures (*curved arrow*) leaving areas of relatively stagnant flow, or at times, actual reversed flow in the lesser curvature (*large arrow*). During diastole, the central dye streams impact on the wali slightly more proximally. Better seen on the super VHS video recording is an apparent compression of the helical dye streams, giving the appearance of a slightly compressed spring, which then elongates during the more rapid flow of systole.

Fig. 5. Flow at the confluence of the vertebral arteries seen with isobaric dye streams. There is slight asymmetry of flow because of the unequal size of the parent vessels. Helical flow is present with the more central dye streams crossing each other and, in this specimen, rotating clockwise when seen from below. After a few vessel diameters, the flow continued through the straight basilar artery and resumed a pattern that was essentially laminar.

Fig. 6. Flow at the distal basilar artery and the aneurysm seen with isobaric dye streams. Flow within the aneurysm was exceedingly complex. The dye stream from the left side of the artery (*red*) passes to the posterolateral wall of the aneurysm, whereas that from the right (*blue*) passes to the left posterior wall of the aneurysm. During systole, high-speed flow along the posterior wall proceeds toward the dome, where it encounters relatively stagnant blood. In this region, it is easier to see the swirls. These swirls then pass down toward the anterior portion of the neck of the aneurysm and during the next systole exit into the posterior cerebral arteries and the right superior cerebellar artery. During diastole, flow is considerably slower but still antegrade, and the swirls in the body and the dome of the aneurysm are easier to see.

an increase in fluid velocity. The collection of dye streams then continued superiorly along the posterolateral wall of the aneurysm until reaching a point near the apex where swirls of dye streams were formed. The swirls then moved from the apex toward the center of the aneurysm. During this migration the swirls became progressively more disordered and smaller to the point where, at end diastole, they rested at the openings of the posterior cerebral arteries at the base of the aneurysm. This transition pattern from the aneurysm neck to the apex and then back to the neck was repeated with each cardiac cycle. At end diastole the collection of disordered swirls, resting at the openings of the posterior cerebral arteries, was ejected by the systolic pulse into both proximal posterior cerebral arteries.

MRA Studies

We will describe the MRA findings beginning with the area of greatest interest, the aneurysm.

Areas of Low Signal

The most striking difference between the 2-D time-of-flight, 3-D time-of-flight, and 3-D phase-contrast images is the signal intensity of the aneurysm (Fig 7). Both time-of-flight techniques show the aneurysm. There are differences in the signal intensities within the aneurysm between

the two time-of-flight techniques with relatively more signal within the aneurysm on the 2-D time-of-flight images. The 3-D time-of-flight images depict the margins of the aneurysm with greater clarity, probably because of the higher spatial resolution of this sequence (1.0 mm versus 1.5 mm). On the 3-D phase-contrast images the signal within the aneurysm is low with the exception of the area at the neck of the aneurysm.

The proximal portions of the posterior cerebral arteries are best seen on the 3-D time-of-flight images (Fig 7). On the 2-D time-of-flight images this segment of the vessel is faint and appears larger in caliber on the anteroposterior projection. However, this is not the case on the axial images through this area (Fig 8). On the lateral projection (Fig 9) the vessel is obscured by overlapping ghosts which degrade the image. The 3-D phase contrast images also show this segment of the artery faintly (Fig 9). However, the arteries appear smaller in diameter than on the 2-D time-of-flight images and more similar to the caliber seen on the 3-D time-of-flight images, although the margins of the arteries are difficult to ascertain because of faint signal. The corresponding 3-D phase-contrast axial images (Fig 8) do not corroborate the appearance of the posterior cerebral arteries on the maximal intensity projection.

The right superior cerebellar artery is seen with certainty only on the 3-D time-of-flight images, probably because of the higher resolution capabilities of this pulse sequence (Figs 7 and 9).

On the 3-D phase contrast images the basilar artery is narrower than the same segment of the model on the time-of-flight sequences. This is not confirmed on the axial images before the maximal intensity projection reconstruction.

The confluence of the two vertebral arteries and the straight portion proximal to this point were best seen on the 3-D time-of-flight sequence (Fig 10). The outer margins of these arteries were irregular and less distinct with areas of focal loss of signal on the 2-D time-of-flight images. More specifically, a minor smooth narrowing of the caliber of the left vertebral artery as it joined the basilar artery was exaggerated when compared with the 3-D time-of-flight images.

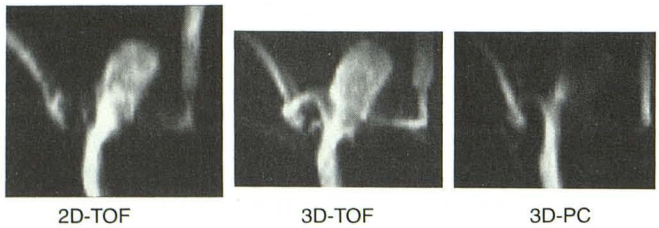

Fig. 7. Maximal intensity projection angiograms (anteroposterior projections) through the model aneurysm. These images are enlargements of those shown in Figures 9 and 10. Acquisition parameters are given in Table 1. TOF indicates time-of-flight; PC, phase contrast.

The complex anatomy of the two compound curves that the vertebral arteries make at the cervical flexures on 2-D time-of-flight images has lower signal in the transverse segments than the flow in the proximal segment (Fig 10). We did not find this on the 3-D time-of-flight images. The signal in these segments of the vertebral arteries on the 3-D phase contrast images is decreased throughout with the exception of the segment proximal to the loop in the right vertebral artery. Although the artery in this segment appears straight on the projection seen in Figure 10, the artery actually curves in and out of the plane of the page.

Areas of Bright Signal

The neck of the aneurysm is bright on all sequences in Figure 7. This is most conspicuous on the 3-D phase-contrast images where it is the only portion of the aneurysm which is well seen. This region is also bright on the time-of-flight images but to a lesser degree and in a smaller area. We found another area of bright signal at the confluence of the left vertebral artery with the basilar artery (Fig 10). Again, this area of increased signal intensity is most apparent on the 3-D phase-contrast sequence and continues for a short distance into the basilar artery. In the cervical flexures the only bright area is in the segment immediately proximal to the second curve of the right vertebral artery or in the first curve (Fig 10).

Areas of Geometric Distortion

The basilar artery, in particular the proximal segment, appeared smaller in caliber on the 3-D phase-contrast images (Figs 8 and 9). This appearance is confirmed on the axial images through this segment of the arteries. Another area of apparent narrowing of the caliber of a vessel is the straight segment of both vertebral arteries before their confluence to form the basilar artery on the 3-D phase-contrast images (Figs 8 and 10). In order to test whether these distortions were caused by oblique flow effects the 3-D time-of-flight sequence was repeated with the in-plane phase-encoded and frequency-encoded axes

swapped. The two images are compared in Figure 11. Note that there is no apparent narrowing of the vertebral artery on the swapped images, and also that the loop of the vessel is more circular on the swapped image.

Pulsatility Artifacts

With pulsatile flow, velocity will vary at different points in the cardiac cycle. There are ghost artifacts on each of the imaging sequences (Fig 9). However, they degrade the 2-D time-of-flight images the most where they overlap the vessel at several points, obscuring the vessel lumen. The ghosts are not apparent on the anteroposterior projection of the 2-D time-of-flight sequence because they occur in the phase-encoding direction, that is, along the axis that would come out of the page. Therefore the ghosts actually overlie each other. On the 3-D time-of-flight images the spacing of the ghosts is much larger, so they do not interfere with the vessel. Also, the ghosts are shifted at a slight angle. As a result, on the anteroposterior projection the ghosts do not perfectly overly the vessel. On the 3-D phase-contrast images this is more pronounced; the ghosts are shifted along a more steeply angled line and are clearly seen as separate from the vessel in the anteroposterior projection proximal to the confluence. In addition, the intensity of the ghosts is brighter in certain segments of the arteries. Specifically, at the aneurysm and at the confluence of the vertebral arteries the ghosts are most intense.

Quantitative MR Velocity Measurements

Quantitative studies with 2-D cine phase contrast were performed in the axial plane at two levels in the model: 1) at the straight segment of the vertebral arteries proximal to the cervical flexures, to calculate volume flow rates for comparison with the flow that was measured using the electromagnetic flow meter; and 2) through the aneurysm, to try to clarify the complex flow in this region (Figs 12, 13, and 14A).

For the section through the proximal section of the vertebral arteries the velocity encoding

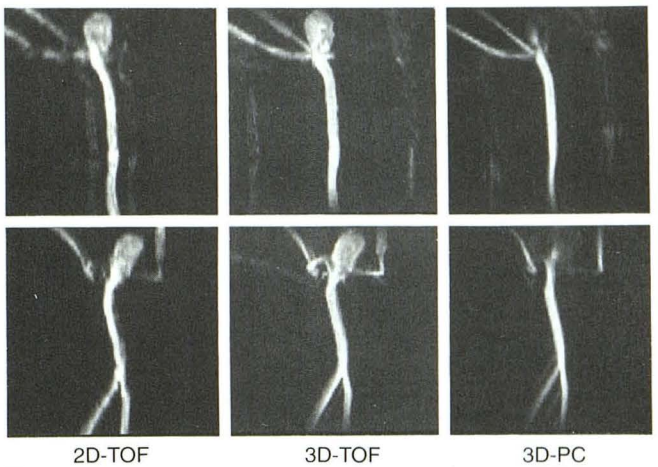

Fig. 9. Maximal intensity projection angiograms of the upper half of the model showing two projections 90° apart for each imaging method. *Top*, lateral projection; *bottom*, anteroposterior projection. Image acquisition parameters are given in Table 1.

Fig. 10. Maximal intensity projection angiograms of the vertebrobasilar model acquired with the acquisition parameters given in Table 1. The 2-D time-of-flight data set was acquired in one acquisition, and for the 3-D data the upper and lower halves of the model were imaged separately and then combined.

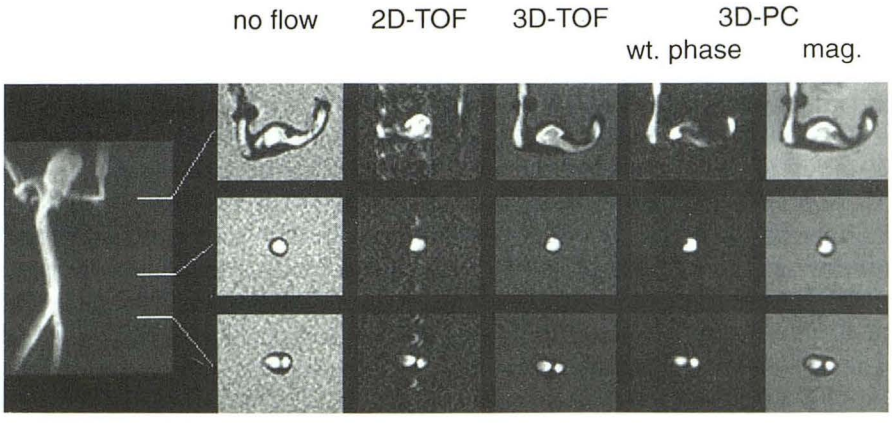

Fig. 8. A composite image showing selected axial sections through the model for three types of acquisitions: 2-D time-of-flight, 3-D time-of-flight, and 3-D phase contrast. For the 3-D phase-contrast data both the weighted phase and magnitude images are shown. The no-flow image (made after the pump was turned off) was acquired with a 2-D time-of-flight sequence with the parameters of Table 1 except that the section thickness was 1.5 mm. The maximal intensity projection angiogram on the *left* (made from the 3-D time-of-flight data set) shows the locations of the axial sections.

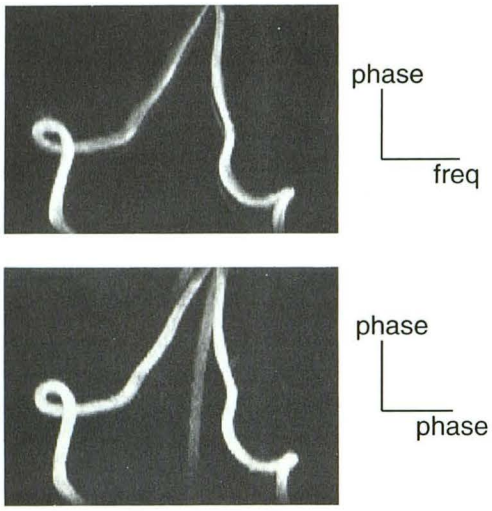

Fig. 11. Two maximal intensity projection angiograms of the cervical flexure region with identical acquisition parameters (3-D time-of-flight [Table 1]) except that the phase- and frequency-encoding axes in the axial plane were swapped. The addition vessel appearing in the *bottom image* is a fluid return line that is aliased into the field of view. Oblique flow artifacts can be seen in the *top image* because the two axes (phase and frequency) are encoded at slightly different times. The inner edge of the angled straight vertebral segment is bright, the vessel appears narrowed, and the circular projection of the cervical flexure is distorted into an oval shape. These effects disappear in the lower image because the two axes of the projection were encoded at the same time.

equaled 100 cm/sec, and only motion in the superior/inferior direction was encoded in the phase of the signal. The 32 phase images corresponding to 32 points in the pump cycle were automatically scaled to velocity units (mm/sec) before analysis. Total volume flow (mL/sec) through each vessel was calculated as described in Materials and Methods. The resulting curves are shown in Figure 14, along with the curve measured with the flow meter. The quantitative agreement was good, suggesting that the region-of-interest selection did not lead to significant overestimation of flow.

For the 2-D cine phase-contrast data through the aneurysm velocity encoding equaled 80 cm/sec and the 32 images were processed somewhat differently to reveal the basic flow patterns. Figure 12 shows the no-flow image through the aneurysm on the left for anatomic orientation. On the right is the average of the 32 velocity images in which bright pixels reflect high average velocities in the superior direction. There is a small bright well-defined region of in-flow on the anatomic right side and also lower velocity inflow around the margin of the aneurysm. There is outflow in the central region. In order to illustrate the time dependence of the velocity in these regions, curves of velocity versus time for small regions of interest in the center, the jet, and the margin of the aneurysm are shown in Figure 13. We also plotted a velocity curve from the stationary background averaging over the same size region of interest in order to gauge any random variations.

Discussion

Understanding the basic physiology and pathology of flow in human vessels is important for understanding the pathogenesis of disease states such as atherosclerosis and berry aneurysm formation (22). The intrinsic flow sensitivity of MR imaging makes it a potentially powerful tool for noninvasively investigating blood flow in the human body. However, earlier investigators have found that many MR angiographic techniques are fraught with artifacts owing to the complex flow patterns in the human vasculature (23–25). These artifacts pose a serious problem in the interpretation of vascular images. Our goal in this study was to correlate vascular flow patterns in a realistic model with the appearance of the same vessels on MRA, so that not only would we be aware of the pitfalls of interpretation of MRA, but we could then hope to find solutions for avoiding artifacts and thereby accurately resolve both the anatomy and the flow physiology of the human vasculature with this powerful tool.

When the model was imaged with an MRA pulse sequence (3-D time-of-flight) with no flow, the signal intensity in the vessel was uniform throughout the model. But with a physiologically realistic pulsatile flow there were substantial signal variations within the vessel with all of the MRA pulse sequences.

Areas of signal variation on the time-of-flight techniques can be attributed to several factors, some of which are caused by the acquisition technique and some also by the projection method used (23). These sequences depend on flow-related contrast caused by the generation of strong signals from unsaturated moving protons entering the image volume and the relative suppression of signal from stationary tissues (26). In conditions in which slow flow exists, the blood remains in the section longer and is subject to a greater number of radio frequency pulses, as are the adjacent soft tissues. The signal intensity of blood then becomes more similar to stationary tissues (26). Saturation effects are reduced by

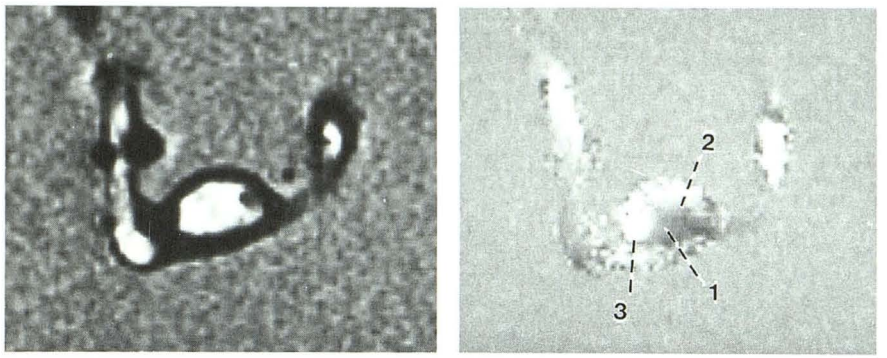

Fig. 12. Quantitative velocity data measured in the aneurysm. On the *left* is a section through the aneurysm with no flow (from a 3-D time-of-flight data set) for anatomic orientation. The *dark circular region* in the margin of the aneurysm is an air bubble which was trapped after the flow was turned off. Similar dark circular regions are seen outside the vessels and are bubbles trapped within the gel surrounding the model. On the *right* is the average phase image from the 2-D cine phase-contrast data set calculated by averaging the 32 images through the pump cycle. Bright signal indicates high velocity in the superior direction (into the aneurysm). Quantitative velocity curves for single pixels in three regions of the aneurysm are shown in Figure 13.

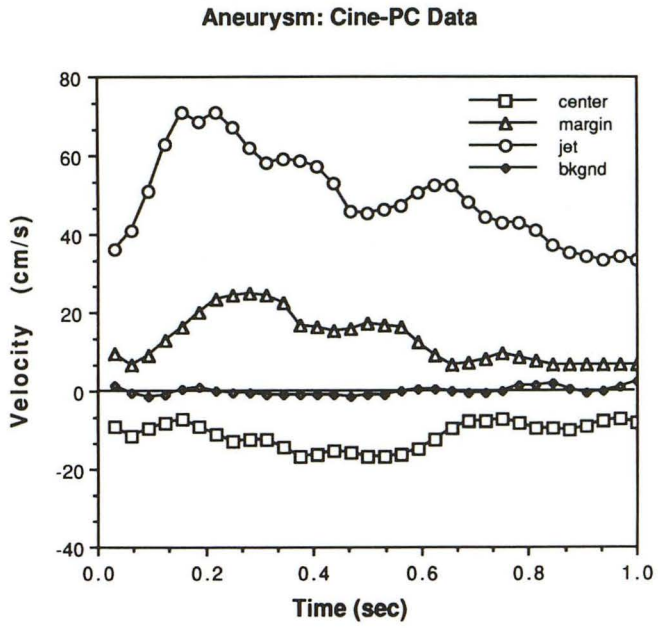

Fig. 13. Quantitative velocity curves from the 2-D cine phase-contrast data set for small regions of interest in three regions in the aneurysm and in a stationary background region. Each region of interest included four pixels. The locations of the regions of interest in the aneurysm are shown in Figure 12 (1, center; 2, margin; 3, jet).

reducing the flip angle, because a large flip angle will produce strong saturation with fewer radio frequency pulses. This saturation effect is particularly prominent when the vessel is in the plane of section so that spins in this vessel are exposed to the radio frequency pulses longer than if the vessel were perpendicular to the plane of section. This phenomenon is called *in-plane saturation*. In-plane saturation is most evident in 2-D time-of-flight, which uses a large flip angle, and can be seen in the vessel in the cervical flexures and the posterior cerebral arteries. In the 3-D time-of-flight images a much smaller flip angle was used (20° instead of 60° in the 2-D time-of-flight), and saturation effects are thus not as prominent. The 3-D phase-contrast images are not as sensitive to saturation effects because the dominant contribution to the weighted phase image is the velocity-dependent phase image.

Apparent signal loss can also occur with time-of-flight techniques because of intravoxel phase cancellation when the first order flow compensation gradient wave forms do not eliminate flow-induced phase changes in the signal. This can occur where there are orders of motion higher than velocity (acceleration and jerk) such as in regions of disordered or complex flow. The phase-contrast techniques are likely to be more sensitive to intravoxel phase cancellations because of the velocity-sensitizing gradients used. The magnetization at each point acquires a phase proportional to its velocity, so spatial averaging of complex flow patterns may lead to signal loss. The weighted phase image may then show a reduced signal intensity which could be misinterpreted as indicating a low average velocity.

All of the MRA images show signal loss within the aneurysm to a variable degree. The flow visualization study demonstrated dye stream flow around the margin of the aneurysm to the apex where the dye streams degenerated into collapsing swirls which eventually exited at the aneurysm neck. Decreased signal within the aneurysm on the 3-D phase-contrast can be attributed to slower velocity and intravoxel dephasing within the areas of disturbed flow. From our quantitative 2-D cine phase-contrast data (Fig 13), the velocity at the margin and at the center is less than 20 cm/sec. Using a smaller V_{enc} (less than 80 cm/

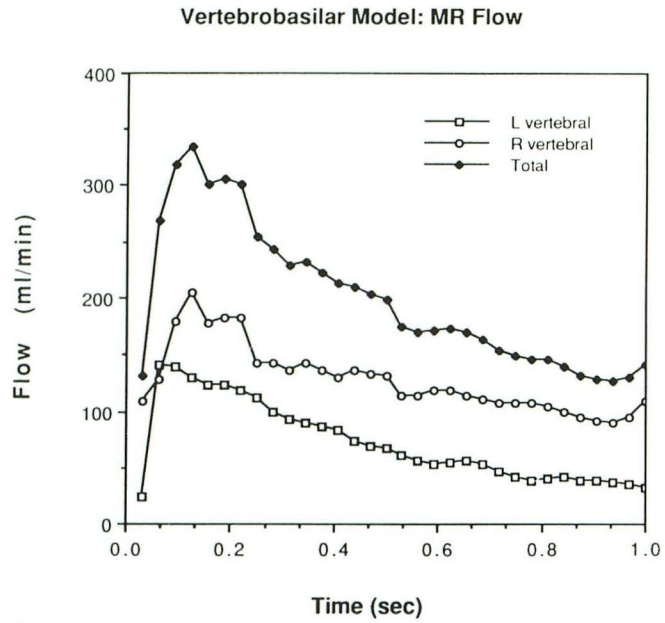

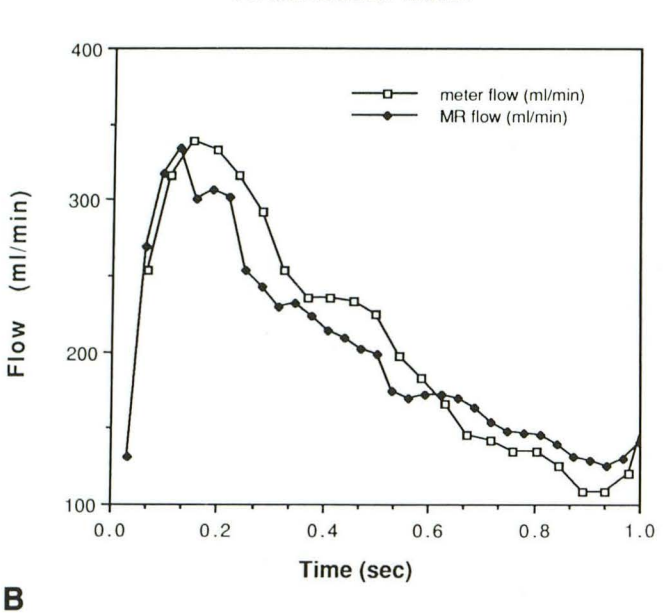

Fig. 14. *A*, Time-resolved total flow measured through the proximal straight segments of the left and right vertebral arteries using the 2-D cine phase-contrast pulse sequence. The sum of the flow in each artery is also graphed.

B, A graph of the sum of the flow measured in each artery with 2-D cine phase-contrast compared with the total flow measured with a flow meter during a single cardiac cycle at another location using identical conditions.

sec) may have shown the aneurysm to better advantage. The aneurysm's containing some signal on both of the time-of-flight sequences suggests that first-order flow compensation is sufficient to prevent signal loss from pulsatile and disordered flow. The 3-D time-of-flight images depict the margins of the aneurysm with greater clarity than the 2-D time-of-flight images owing to the higher resolution capabilities of the 3-D acquisition in one plane (1.0 mm with 3-D compared to 1.5 mm with 2-D).

There was no signal loss apparent in the basilar artery or the confluence of the two vertebral arteries. This is to be expected because the flow visualization studies did not demonstrate any disturbed flow in these segments of the model.

The images also reveal several areas of increased signal intensity. At the neck of the aneurysm on the 3-D phase-contrast images there is a tear drop–shaped area of brightness that corresponds to an area where the dye streams are crowded on the flow visualization studies. Increased flow velocity at this site would explain both the increase in signal intensity and the dye stream crowding. The 2-D cine phase-contrast quantitative velocity images confirm that the velocity is increased focally. This would correspond to an angiographic jet. The 2-D cine phase-contrast also shows a region of moderate inflow in the outer margin of the aneurysm (Fig 12). On the model flow study this area was seen as a dye stream that continued upward from the jet at the aneurysm neck and flowed rapidly around the wall of the aneurysm to the apex. At this point the dye stream formed a swirl which gradually migrated to the base of the aneurysm. Referring to the 2-D cine phase-contrast image in Figure 12, the region of the slower flowing swirl corresponds to the central outflow region where the velocity is in the opposite direction to that in the jet and the inflowing outer margin. Moreover, comparing the velocity curves of the small regions of interest from each of these three locations in the aneurysm (Fig 13), a number of observations can be made. The overall trend of the three curves is for velocity to increase and then decrease in the jet and along the margin of the aneurysm. The curves show a slight delay between the peak inflow in the jet and in the margin (Fig 13). The velocity at the center of the aneurysm is negative. This indicates that the flow is in the opposite direction to the other two sites, that is, out of the aneurysm. The velocity at the center of the aneurysm is both lower in magnitude and less variable than that in the jet. It may be that the average velocity in the center is decreased because the energy of the flowing fluid is dissipated as the fluid swirls at this location.

The 2-D cine phase-contrast technique clearly shows the different velocity characteristics in the different regions. The curve of the velocity from the stationary background region demonstrates that random variations in the measured velocity are significantly smaller than the velocity variations measured in the aneurysm.

A similar region of brightness at the site of the jet is seen on both time-of-flight acquisitions. However, the area of increased signal intensity is smaller in diameter and continues in a line along the aneurysm wall for a short distance particularly on the 3-D time-of-flight images. Two factors may contribute to the brighter signal in this region. First, the faster average velocity found in the cine phase-contrast data suggests that there may be a greater refreshment of inflowing spins than in the nearby slower flowing regions of the aneurysm. Second, the structure of the jet may be more coherent than the more disordered flow found in the central region in the flow visualization studies. As a result, the effects of the intravoxel phase incoherence may be less severe in the region of the jet.

Another region of brightness is seen at the confluence of the left vertebral artery with the basilar artery. The bright signal continues for a short distance into the basilar artery on the 3-D phase-contrast images. The flow visualization studies in this region show crowding of the dye streams. The increased velocity implied by the crowded dye streams would explain the bright signal on the 3-D phase-contrast images. In addition, the apparent narrowing of the basilar artery on the 3-D phase-contrast images (Figs 8 and 9), when compared with the time-of-flight images, also reflects the increased velocity because of a concentration of the flow in a small cross-section. The factors described above, which may contribute to the bright time-of-flight signal in the aneurysm neck, may also apply to this region.

In our MR studies we found several examples of vessel distortion which can be attributed to oblique or curved flow effects. In 3-D imaging the encoding of spatial position along the phase-encoded axes occurs earlier than the encoding of position along the frequency-encoded axis (27). As a result, any motion of the blood in the interval between the phase-encoding pulses and the echo center will lead to mismapping of the blood signal in the reconstructed image. The resulting geometric distortions may involve a change in the caliber of a vessel, displacement of signal to one side of the vessel, or distortions of the shape of curved vessels (28). As shown in Figures 10 and 11, these distortions occur only when viewing a plane in which one axis is phase encoded and the other is frequency encoded, and the vessel orientation is oblique to both axes. These effects have been analyzed in earlier work (27, 28). The upper image of Figure 11 shows a bright signal within the outer wall of the first curve of the cervical flexure and apparent narrowing of the straight segment of the right vertebral artery combined with a bright inner edge. In this image the vertical axis is phase encoded, and the horizontal axis is frequency encoded. When this 3-D time-of-flight acquisition was repeated with the in-plane phase and frequency encoded axes swapped, both axes in the maximal intensity projection of Figure 11 are phase encoded. Because these two axes are spatially encoded at the same time, there are no distortions of the vessel. Note also that the loop of the cervical flexure is distorted from a roughly circular shape (Fig 11, *bottom*) to a more oval shape (Fig 11, *top*) because of the curved flow, consistent with an earlier analysis of distortions caused by curved flow (28).

Ghost artifacts caused by the pulsatile flow in the model occurred in all of our imaging studies, although the appearance of the ghosts varied substantially between pulse sequences. Pulsatility artifacts arise from variations in either the magnitude- or the flow-generated phase of the MR signal (24, 25, 27, 29). The structures of pulsatility artifacts in 2-D and 3-D MRA were analyzed in detail in two recent papers (27, 30). Specifically, ghosts are shifted along each phase-encoded axis a distance proportional to the pulsation frequency and the time between successive phase-encoding steps along that axis. For 2-D time-of-flight, there is only one phase-encoded axis and the time between phase-encoding steps is simply repetition time. The resulting ghosts are close to the vessel and in our studies overlapped the vessel in some sections.

In 3-D imaging, ghosts are shifted along both phase-encoded directions and can be seen to be displaced at a slight angle in the maximal intensity projection directions showing the Y-Z plane. The shift in the Y direction is much greater than the shift in Z because the time between phase-encoding steps is longer by a factor of N_z, the number of phase-encoding steps in Z. The ghost displace-

ment is often larger than the field of view, resulting in wraparound (aliasing). In the 3-D phase-contrast images, the angle of the ghosts is more pronounced because the time between phase-encoding steps is increased by a factor of four (for each step, four excitations are required for velocity sensitivity along all three axes). The apparent angle of ghost propagation is increased because of the resulting high degree of wraparound.

In this paper we have described the use of a clear silicone model of the human vertebrobasilar system to study flow patterns and correlate these patterns with the MRA images obtained with 2-D time-of-flight, 3-D time-of-flight, and 3-D phase-contrast pulse sequences. The dye stream patterns we observed are extremely complex and sometimes variable. It is reasonable to assume that flow patterns will have individual variability for each vessel in each human as well. Nevertheless, the general patterns revealed in our model flow studies helped to clarify the different MR appearances of these vessels and the image artifacts. We also found that 2-D cine phase contrast can accurately quantitate simple pulsatile flows providing time-resolved volume flow rates which are in good agreement with electromagnetic flow meter recordings. These results complement other recent evaluations of the accuracy of phase-contrast methods (31, 32). More complex flow patterns, such as those which occur in aneurysms, can also be assessed with this technique though their interpretation is more problematic. MR imaging, although subject to a number of artifacts related to the underlying flow pattern, provides a safe, noninvasive tool with which we can directly obtain true physiologic information, determine global flow volumes, and even see high-velocity streaming. This new knowledge will assist us with future investigations of the many arterial degenerative diseases.

Acknowledgments

We thank Ms. Kim Knox for creating the models and Ms. Marsha Earnshaw for her photographic assistance.

References

1. Kerber CW, Heilman CB. Flow dynamics in the human carotid artery: I. Preliminary observations using a transparent elastic model. *AJNR Am J Neuroradiol* 1992;13:173–180
2. Liepsch DW. Flow in tubes and arteries: a comparison. *Biorheology* 1986;23:395–433
3. Liepsch DW, Morabec ST. Pulsatile flow of non-Newtonian fluid in distensible models of human arteries. *Biorheology* 1984;21:571–586
4. Mann DE, Tarbell JM. Flow of non-Newtonian blood analogue fluids in rigid curved and straight artery models. *Biorheology* 1990;27:711–733
5. Fei DY, Kraft KA, Fatouros PP. Model studies of nonsteady flow using magnetic resonance imaging. *J Biomech Eng* 1990;112:93–99
6. Caro CG, Parker KH. Mechanics and imaging of the macrocirculation. *Magn Reson Med* 1990;14:179–186
7. Masaryk TJ, Ross JS, Modic MT, et al. Carotid bifurcation: MR imaging. *Radiology* 1988;166:461–466
8. Masaryk AM, Ross JS, DiCello MC, et al. 3DFT MR angiography of the carotid bifurcation: Potential and limitations as a screening examination. *Radiology* 1991;179:797–804
9. Litt AW, Eidelman EM, Pinto RS, et al. Diagnosis of carotid artery stenosis: comparison of 2DFT time of flight MR angiography in 50 patients. *AJNR Am J Neuroradiol* 1991;12:149–154
10. Ross JS, Masaryk TJ, Modic MD, et al. Magnetic resonance angiography of the extracranial carotid arteries and intracranial vessels: a review. *Neurology* 1989;39:1369–1376
11. Masaryk TJ, Modic MT, Ruggieri PM, et al. Three-dimensional (volume) gradient-echo imaging of the carotid bifurcation: preliminary clinical experience. *Radiology* 1989;171:801–806
12. Alfidi RJ, Masaryk TJ, Haacke EM, et al. MR angiography of peripheral, carotid, and coronary arteries. *AJR Am J Roentgenol* 1987;149:1097–1109
13. Ross JS, Masaryk TJ, Modic MT, et al. Intracranial aneurysms: evaluation by MR angiography. *AJNR Am J Neuroradiol* 1990;11:449–456
14. Sevick RJ, Tsuruda JS, Schmalbrock P. Use of 3D time of flight magnetic resonance angiography in the evaluation of intracranial aneurysms. *J Comput Assist Tomogr* 1990;14:874–881
15. Tsuruda JS, Shimakawa A, Pelc NJ, et al. Dural sinus occlusion: Evaluation with phase- sensitive gradient-echo MR imaging. *AJNR Am J Neuroradiol* 1991;12:481–488
16. Edelman RR, Wentz KU, Mattle HP, et al. Intracerebral arteriovenous malformations: evaluation with selective MR angiography and venography. *Radiology* 1989;173:831–837
17. Walker MF, Souza SP, Dumoulin CL. Quantitative flow measurement in phase contrast MR angiography. *J Comput Assist Tomogr* 1988;12:304–313
18. Pelc NJ, Herfkens RJ, Shimikawa A, et al. Phase contrast cine magnetic resonance imaging. *Magn Reson Quart* 1991;7:229–254
19. Kerber CW, Heilman CD, Zanetti PH. Transparent elastic arterial models: I. A brief technical note. *Biorheology* 1989;26:1041–1049
20. Gullberg GT, Wehrli FW, Shimakawa A, et al. MR vascular imaging with a fast gradient refocusing pulse sequences and reformatted images from transaxial sections. *Radiology* 1987;165:241–146
21. Pedley TJ. *The fluid mechanics of large blood vessels.* Cambridge: Cambridge University Press, 1980:160
22. Gonzalez CF, Cho YI, Ortega HV, et al. Intracranial aneurysms: flow analysis of their origin and progression. *AJNR Am J Neuroradiol* 1992;13:181–188
23. Tsuruda J, Saloner D, Norman D. Artifacts associated MR neuroangiography. *AJNR Am J Neuroradiol* 1992;13:1411–1422
24. Wood ML, Henkelman RM. MR image artifacts from periodic motion. *Med Phys* 1985;12:143–151
25. Haacke EM, Patrick JL. Reducing motion artifacts in 2D fourier transform imaging. *Magn Reson Imaging* 1986;4:359–376
26. Haacke EM, Masaryk TJ, Wielopolski PA, et al. Optimizing blood vessel contrast in fast three-dimensional MRI. *Magn Reson Med* 1990;14:202–221
27. Frank LR, Buxton RB, Kerber CW. Pulsatile flow artifacts in 3D magnetic resonance imaging. *Magn Reson Med* 1993;30:296–304

28. Frank LR, Buxton RB. Distortions from curved flow in magnetic resonance imaging. *Magn Reson Med* 1993;21:84–93
29. Perman WH, Moran PR, Moran RA, et al. Artifacts from pulsatile flow in MR imaging. *J Comput Assist Tomogr* 1986;10:473–483
30. Buxton RB, Kerber CW, Frank LR. Artifacts in 2D time-of-flight magnetic resonance angiography: initial studies in elastic models of the human carotid bifurcation. *J Magn Reson Imaging* 1993;3: 625–636
31. Meier D, Maier S, Bosiger P. Quantitative flow measurements on phantoms and on blood vessels with MR. *Magn Reson Med* 1988;8:25–34
32. Sondergaard L, Stahlberg F, Thomsen C, et al. Accuracy and precision of MR velocity mapping in measurements of stenotic cross-sectional area, flow rate, and pressure gradients. *J Magn Reson Imaging* 1993;3:433–437